Evaporite weathering and deposition as a long-term climate forcing

Graham A. Shields[1*] and Benjamin J.W. Mills[2]

[1]Department of Earth Sciences, University College London, Gower Street, London WC1E 6BT, UK;
*corresponding author: g.shields@ucl.ac.uk
[2]School of Earth and Environment, University of Leeds, Leeds LS2 9JT, UK

Abstract

Although it is widely accepted that Earth's long-term surface temperature is regulated by the mutual dependence of silicate weathering and climate on CO_2, the root causes of some climatic events remain unresolved. We show here for the first time that imbalances between evaporite weathering and deposition can affect climate through the process of carbonate sedimentation. Calcium sulfate weathering supplies Ca^{2+} ions to the ocean unaccompanied by carbonate alkalinity, so that increased carbonate precipitation strengthens greenhouse forcing through transfer of CO_2 to the atmosphere. Conversely, calcium sulfate deposition weakens greenhouse forcing, while the high depositional rates of evaporite giants may overwhelm the silicate weathering feedback, causing several degrees of planetary cooling. Non-steady state evaporite dynamics and related feedbacks have hitherto been overlooked as drivers of long-term carbon cycle change. Here we illustrate the importance of evaporite deposition, in particular, by showing how a series of massive depositional events contributed to global cooling during the mid-late Miocene.

Introduction

"*Carbon dioxide partial pressure and Earth's greenhouse effect are … buffered by the temperature dependence of the rate of carbon dioxide consumption in the weathering of silicate minerals*" (Walker et al., 1981). This canonical negative feedback is still our best explanation for how Earth's long-term surface temperature resists external forcing, such as changes in solar luminosity or CO_2 outgassing. However, despite broad agreement around the operation of Earth's natural thermostat, some features of Earth's climate history, notably abrupt hyperthermal or cooling events, imply weakening of the silicate weathering buffer.

One inherent assumption of the silicate weathering feedback is that the calcium input to the ocean is balanced by carbonate deposition on long time scales, i.e. $>10^5$ years. The stoichiometric equivalence between the Ca (and Mg) (Berner, 1991) released from silicate weathering and the Ca removed through carbonate deposition has long been known to buffer the long-term carbon cycle (Berner, 2012). However, the riverine Ca + Mg dissolved load integrates contributions from three different lithologies: carbonates, silicates and evaporites, which have contrasting effects on the carbon cycle (Figure 1 and Equations 1-3). Carbonate minerals dissolve quantitatively (Eq. 1), and release calcium ions and carbonate alkalinity to the ocean, with one mole of bicarbonate sourced from the rock reservoir and one from the atmosphere. Although carbonate weathering transfers CO_2 from the atmosphere to the ocean, it does not affect the long-term carbon balance because subsequent carbonate burial (reverse of Eq. 1) effectively recombines these constituents and releases CO_2.

$$CaCO_3 + CO_2 + H_2O \leftrightarrows Ca^{2+} + 2HCO_3^- \qquad (1)$$

Silicate minerals undergo incongruent leaching during chemical weathering (Eq. 2), resulting in the release of cations and carbonate alkalinity to the ocean, but with carbon entirely derived from the atmosphere. This drawdown of CO_2 exceeds that released during carbonate precipitation, and thus coupled silicate weathering and carbonate burial results in a net transfer of carbon from the surface system into the sediments.

$$CaSiO_3 + 2CO_2 + H_2O \rightarrow Ca^{2+} + 2HCO_3^- + SiO_2 \qquad (2)$$

Finally, non-carbonate evaporite minerals like gypsum (Eq. 3) dissolve rapidly and entirely, releasing cations (e.g. Na^+, Mg^{2+}, Ca^{2+}, K^+) and anions (halides, sulfates) into rivers unaccompanied by carbonate alkalinity, for example:

$$CaSO_4 \cdot 2H_2O \rightarrow Ca^{2+} + SO_4^{2-} + 2H_2O \qquad (3)$$

In established long-term biogeochemical models (Berner, 1991; Lenton et al., 2018; Mills et al., 2018), evaporite fluxes are negated by assuming a close balance between the weathering and deposition of Ca- and Mg-bearing evaporite minerals on all time scales. However, the largest, basin-scale or giant evaporite deposits formed sporadically due to the restriction of marginal ocean basins, most commonly during basin closure or rifting (Warren, 2010). Unlike

carbonate or silicate lithologies, evaporites are also unevenly distributed geographically and are of variable chemical and mineralogical composition, meaning that the relative contribution of evaporites to global Ca and Mg fluxes varied greatly over Earth history (Wortmann and Paytan, 2012). Due to the regional distribution of rare evaporite giant deposits, imbalance between evaporite, and specifically calcium sulfate, weathering and deposition must have occurred on up to 10^7-year time scales since the onset of oxidative pyrite weathering after the Great Oxidation Event.

Evaporite giant deposition and weathering during the Cenozoic Era

The last evaporite giant formed episodically between 5.97 and 5.33 million years ago (Meilijson et al., 2019) due to restriction of the Mediterranean Sea during the Messinian Salinity Crisis (MSC). The MSC followed evaporite deposition in the Red Sea during the preceding Tortonian Age and brought to an end evaporite deposition across Eurasia spanning the entire Miocene Epoch (Rohais et al., 2016; Mandic et al., 2019) (Figure 2). The first giant evaporite deposits of the Cenozoic Era were particularly gypsum-rich (Al-Juboury and McCann, 2008), due primarily to precipitation from sulfate-rich seawater (Halevy et al., 2012; Zeebe and Tyrrell, 2019), and formed as a result of the restriction of the Mesopotamian and Paratethyan seaways during Langhian (c. 15.97-13.65 Ma) (Al-Juboury and McCann, 2008) and early Serravalian (c. 13.6-13.0 Ma) (De Leeuw et al., 2010) times, respectively. Miocene evaporite deposits formed predominantly, therefore, in two episodes (c. 16-13 Ma and c. 9-5 Ma) that delimit the only evaporite giants of the last 120 million years (Warren, 2010).

With the exception of these two mid-late Miocene intervals, evaporite weathering likely outpaced deposition for most of the Cenozoic Era. Moreover exceptionally high rates of evaporite weathering likely occurred following the initial phase of Himalayan collision in the early Eocene (Wortmann and Paytan, 2012), which records a rise in seawater $\delta^{34}S$ beginning c. 53 Ma (Yao et al., 2020). This weathering event and the later deposition events are shown in Figure 2, and are plotted against global average surface temperature as inferred from benthic foraminiferal oxygen isotopes (Zachos et al., 2008; Hansen et al., 2013). While it is difficult to constrain the precise timing of evaporite weathering events during the early Eocene, the timings of evaporite deposition during the Langhian-Serravallian and Tortonian-Messinian are much better known, and both coincide with episodes of major global cooling and ice sheet expansion (Holbourn et al., 2018; Bialik et al., 2019).

Evaporite forcing of climate change

Here we define and demonstrate a mechanism by which massive evaporite events may contribute to shifts in climate. The events drive non-steady-state marine inventories of calcium, with implications for the net burial of calcium carbonate, and thus ocean carbonate chemistry. The saturation state of calcium carbonate, Ω, depends on the concentration of Ca^{2+} and CO_3^{2-} ions:

$$\Omega = \frac{[Ca^{2+}][CO_3^{2-}]}{K_{sp}} \qquad (4)$$

where K_{sp} is the solubility constant, which is sensitive to temperature, pressure and salinity. Any large increase in the ocean Ca inventory, in the absence of any linked change in alkalinity, should increase $CaCO_3$ burial rates, lower marine pH, and thus release CO_2 to the atmosphere (Zeebe and Tyrrell, 2019). Conversely, evaporite deposition causes [Ca] to decrease and so results in reduced carbonate precipitation, rising alkalinity and gas-transfer of CO_2 into the ocean. Because global marine carbonate burial rates were decoupled from the carbonate compensation depth (CCD) during the Cenozoic (Greene et al., 2019), direct comparison with CCD changes is complex. Ultimately, imbalances in marine alkalinity and $CaCO_3$ burial would be remedied by the response of silicate weathering to changes in CO_2, but the intervening ~10^6 years could see substantial climatic change.

To explore the potential magnitude of the effects of evaporite weathering and burial events on the long-term carbon cycle we modify a recent biogeochemical box model (Dal Corso et al., 2020). The model consists of an atmosphere and three ocean boxes (surface, high-latitude, deep) (Sarmiento and Toggweiler, 1984), has an explicit representation of carbonate chemistry (Walker and Kasting, 1992), and includes the canonical long-term carbon cycle fluxes that are at the heart of current Phanerozoic modelling frameworks (Berner, 2006; Lenton et al., 2018; Krause et al., 2018), whereby carbon is supplied to the surface system via tectonic degassing; silicate and carbonate weathering are dependent on global temperature through reaction kinetics and runoff relationships; and marine carbonate burial depends on $CaCO_3$ saturation state through a power-law relationship, e.g. (Rampino and Caldeira, 2005). A brief summary of the most important equations and a full model derivation are in the SI. The model is designed around a preindustrial steady state and we begin our experiments from a steady state in which

the tectonic CO_2 input rate is increased to 50% higher than the present day. This raises atmospheric CO_2 to ~550 ppm.

Figure 3 shows the response of the model to a calcium sulfate weathering event in which we test the addition of between 10^{13} and 10^{14} moles of Ca per year for 1 million years. This is a maximum estimate intended to test the full scope of system response, and while such large input events may have occurred at points in Earth history (Shields et al., 2019), recent estimates of the mass of sulfate liberated during the Himalayan collision have been revised downwards to around $3 - 4 \times 10^{12}$ moles per year over a longer period (Yao et al., 2020). In the model, over the first 150 kyr of weathering, ocean Ca concentration doubles. This rise in concentration leads to excess $CaCO_3$ burial, which reduces ocean alkalinity and drives a transient sea-to-air flux of CO_2, raising the atmospheric concentration by up to 200 ppm during the period of instability. Stability is regained because ocean acidification reduces $CaCO_3$ burial, and alkalinity is delivered from enhanced continental weathering in a warmer climate. Although the high-end of the calcium input scenario in the model results in an unrealistic 80 mM of Ca after 1 Myr, the peak in CO_2 occurs after only ~150 kyr, when [Ca] is a more modest 20 mM.

In Figure 4 we test an evaporite deposition event of between 5×10^{12} and 2×10^{13} moles per year for 1 Myr. We cannot test such large amounts of Ca removal as we can for input because the marine Ca reservoir in our model would be entirely depleted, and the maximal scenario we test has an output rate in line with the Messinian Salinity Crisis (Blanc, 2006), which is considered to have removed $\sim 1.4 \times 10^{19}$ moles of Ca - sufficient to more than halve the modern marine Ca reservoir – assuming that 20% of all deposited evaporite (Blanc, 2006) was in the form of $CaSO_4$ (gypsum, selenite or anhydrite). Estimates for $CaSO_4$ deposition rates during other evaporite giant episodes are comparable, e.g. 1.1×10^{13} moles per year for 2 Myr for the early Cretaceous Aptian event (Wortmann and Chernyavsky, 2007). Evaporite deposition has a more powerful climate impact and cooling effects continue for the duration of the event, rather than being quickly buffered by changes to continental weathering. This is because the shelf sea alkalinity budget is resupplied from the large deep ocean reservoir, somewhat nullifying the reduction in silicate weathering rates caused by climate cooling. Overall, a maximal evaporite weathering event (Figure 3) might result in a ~200 kyr CO_2 spike of 50-200 ppm, but the rate of evaporite weathering during the early Cenozoic implies that the low end of this range is far more likely. In contrast, the Messinian-like forcing we apply results

in a ~50 to ~300 ppm reduction in atmospheric CO_2, which drives ~0.5 to ~6°C of global cooling in the model.

The potential role of evaporites in climate forcing and feedbacks

Although it would be tempting to link enhanced evaporite weathering due to Himalayan collision with short-lived hyperthermal events of the Eocene Epoch, past weathering fluxes are still too poorly constrained to draw any firm conclusions. Relating these model scenarios directly to the geological record evidently requires more detailed study.

In contrast to major weathering during orogeny, major evaporite deposition drives stable cooling throughout events, which are better constrained in terms of timing and magnitude. The first evaporite giants of the Cenozoic Era formed during the stepwise closure of the Mesopotamian Seaway, which terminated around 13.8 Ma, when the onset of permanent glaciation of Antarctica caused global sea levels to fall (Bialik et al., 2019). Thick gypsum deposits formed from ca. 16 Ma (Al-Juboury and McCann, 2008), culminating in the short-lived Badenian Salinity Crisis (De Leeuw et al., 2010) once the Paratethys Ocean became cut off at 13.8 Ma (Langhian-Serravalian boundary). Evaporite deposition thus coincided with an interval of major cooling (Fig. 2), while the relationship between cooling, sea-level fall, basin restriction and evaporite deposition may have acted as a positive feedback reinforcing cooling.

A similar positive feedback can be envisaged towards the end of the Miocene when the main Tortonian phase of anhydrite deposition in the Red Sea and Gulf of Suez (Bosworth, 2015; Rohais et al., 2016) again accompanied global cooling (Herbert et al., 2016). Similarly, the expansion of ice cover in Antarctica to near modern levels by 6.0 Ma is considered to have triggered the Messinian Salinity Crisis (Pérez-Asensio et al., 2013). Messinian cooling was accompanied by intensification of the Asian Winter Monsoon and resulted in the onset of ephemeral Northern Hemisphere glaciations between 6.0 Ma and 5.5 Ma (Holbourn et al., 2018), coinciding with maximal rates of sulfate deposition in the Mediterranean Sea between 5.96 Ma and 5.55 Ma (Cosentino et al., 2013). Total closure of the Mediterranean Sea and deposition of a thick halite layer followed further sea-level drawdown related to the last major period of glacial expansion of the Miocene (TG12), which took place around 5.5 Ma (Speranza et al., 2013). This ‘Messinian Gap’ was then followed by a second, shorter interval of sulfate deposition between 5.50 and 5.33 Ma (Cosentino et al., 2013).

Evaporites contributed conceivably to negative climate feedbacks, too, due to the common association between evaporite giants, warm climates and rifting. Conversely, a weakening of this negative feedback due to low seawater sulfate might have exacerbated global

warming during mass extinctions, e.g. early Cambrian (Botoman), late Devonian, Permian-Triassic, Triassic-Jurassic events, which all followed extensive evaporite deposition (Warren, 2010). Prolonged sulfate deposition would also have exacerbated ocean anoxia due to the oxygen deficit caused by an imbalance between terrestrial sulfide oxidation and marine pyrite burial, a reversal of the oxygen surplus caused by sulfate weathering during ocean oxygenation events of the Neoproterozoic Era (Shields et al., 2019).

Conclusion

Non-steady-state evaporite dynamics have the potential to drive global climate change on long time scales. Although the magnitude of such effects requires case-by-case study, our purpose here has been to demonstrate a new climate mechanism, in which the deposition of evaporite giants, in particular, has the potential to overwhelm the silicate weathering thermostat and force global cooling either directly or via feedbacks between evaporite deposition, climate change and ice sheet dynamics.

Acknowledgements

The authors gratefully acknowledge funding support from a Leverhulme Research Fellowship (RF-2019-435) and NERC grant NE/P013643/1 (BETR programme) to G.A.S. and a NERC grant (NE/S009663/1) and University of Leeds Academic Fellowship to B.J.W.M. We also thank U. Wortmann, O. Bialik and an anonymous reviewer for their constructive comments.

Figure captions

Figure 1. Delivery and removal of marine calcium and carbonate alkalinity. *The three key weathering types are shown in different colours, where multiple arrows represent molar stoichiometry. Carbonate weathering (blue) transfers calcium and carbonate alkalinity from the continental rock reservoir, and CO_2 from the atmosphere, into the ocean. Carbonate deposition (black) reverses this process, removing alkalinity and calcium and releasing CO_2. Silicate weathering (purple) transfers calcium from the rock reservoir to the ocean, and transfers two moles of carbon from the atmosphere to the ocean. Evaporite weathering (yellow) transfers only calcium to the ocean. Note that this is a simplification – see the model derivation for all fluxes and processes.*

Figure 2. Cenozoic global average temperature against evaporite events. *Temperature record from Hansen et al. (2013). The postulated period of evaporite weathering is shown as yellow and known deposition events are shown as vertical teal bars. Horizontal blue bars show the existence of ice caps in the northern and southern hemispheres.*

Figure 3. Model predictions for an evaporite weathering event. *A. Calcium sulfate input is imposed for 1Myr. B. Marine calcium concentration increases substantially. C. A pulse of $CaCO_3$ burial occurs due to increased Ca but is nullified as alkalinity falls. D. Atmospheric CO_2 rises through air-sea exchange as ocean pCO_2 increases. E. Global average surface temperature. Shaded area represents weathering between* 10^{13} *and* 10^{14} *moles per year.*

Figure 4. Model predictions for an evaporite deposition event. *A. Calcium sulfate deposition is imposed for 1Myr. B. Marine calcium concentration decreases substantially. C. A $CaCO_3$ burial is greatly reduced as [Ca] falls. D. Atmospheric CO_2 falls through air-sea exchange as ocean pCO_2 decreases. E. Global average surface temperature. Shaded area represents deposition between* 5×10^{12} *and* 2×10^{13} *moles per year.*

253

254

255 **References**

256 Al-Juboury, A.I., and McCann, T., 2008, The Middle Miocene Fatha (Lower Fars)
257 Formation, Iraq: GeoArabia, v. 13, p. 141–174.
258 Berner, R.A., 1991, A model for atmospheric CO_2 over Phanerozoic time: American Journal
259 of Science, v. 291, p. 339–376, doi:10.2475/ajs.291.4.339.
260 Berner, R.A., 2006, GEOCARBSULF: A combined model for Phanerozoic atmospheric O_2
261 and CO_2: Geochimica et Cosmochimica Acta, doi:10.1016/j.gca.2005.11.032.
262 Berner, R.A., 2012, Jacques-Joseph Ebelmen, the founder of earth system science: Comptes
263 Rendus - Geoscience, v. 344, p. 544–548, doi:10.1016/j.crte.2012.08.001.
264 Bialik, O.M., Frank, M., Betzler, C., Zammit, R., and Waldmann, N.D., 2019, Two-step
265 closure of the Miocene Indian Ocean Gateway to the Mediterranean: Scientific Reports,
266 v. 9, p. 1–10, doi:10.1038/s41598-019-45308-7.
267 Blanc, P., 2006, Improved modelling of the Messinian Salinity Crisis and conceptual
268 implications: v. 238, p. 349–372, doi:10.1016/j.palaeo.2006.03.033.
269 Bosworth, W., 2015, Geological evolution of the Red Sea: Historical background, review,
270 and synthesis, *in* Rasul, N.M.A. and Stewart, I.C.F. eds., The Red Sea, Springer Berlin
271 Heidelberg, p. 45–78, doi:10.1007/978-3-662-45201-1_3.
272 Cosentino, D., Buchwaldt, R., Sampalmieri, G., Iadanza, A., Cipollari, P., Schildgen, T.F.,
273 Hinnov, L.A., Ramezani, J., Bowring, S.A., and Ambientale, G., 2013, Refining the
274 Mediterranean " Messinian gap " with high-precision U-Pb zircon geochronology,
275 central and northern Italy: , p. 323–326, doi:10.1130/G33820.1.
276 Dal Corso, J., Mills, B.J.W., Chu, D., Newton, R.J., Mather, T.A., Shu, W., Wu, Y., Tong, J.,
277 and Wignall, P.B., 2020, Permo–Triassic boundary carbon and mercury cycling linked
278 to terrestrial ecosystem collapse: Nature Communications, v. 11, p. 1–9,
279 doi:10.1038/s41467-020-16725-4.
280 Greene, S.E., Ridgwell, A., Kirtland Turner, S., Schmidt, D.N., Pälike, H., Thomas, E.,
281 Greene, L.K., and Hoogakker, B.A.A., 2019, Early Cenozoic decoupling of climate and
282 carbonate compensation depth trends: Paleoceanography and Paleoclimatology, v. 34, p.
283 930-945, doi:10.1029/2019PA003601.
284 Halevy, I., Peters, S.E., and Fischer, W.W., 2012, Sulfate burial constraints on the

285 Phanerozoic sulfur cycle: Science, v. 337, p. 331-334, doi:10.1126/science.12.20224.
286 Hansen, J., Sato, M., Russell, G., and Kharecha, P., 2013, Climate sensitivity, sea level and
287 atmospheric carbon dioxide: Philosophical Transactions of the Royal Society A:
288 Mathematical, Physical and Engineering Sciences, doi:10.1098/rsta.2012.0294.
289 Herbert, T.D., Lawrence, K.T., Tzanova, A., Peterson, L.C., Caballero-Gill, R., and Kelly,
290 C.S., 2016, Late Miocene global cooling and the rise of modern ecosystems: Nature
291 Geoscience, v. 9, doi:10.1038/NGEO2813.
292 Holbourn, A.E., Kuhnt, W., Lübbers, J., Andersen, N., and Clemens, S.C., 2018, Late
293 Miocene cooling and intensification of southeast Asian winter monsoon: Nature
294 Communications, doi:10.1038/s41467-018-03950-1.
295 Krause, A.J., Mills, B.J.W., Zhang, S., Planavsky, N.J., Lenton, T.M., and Poulton, S.W.,
296 2018, Stepwise oxygenation of the Paleozoic atmosphere: Nature Communications,
297 doi:10.1038/s41467-018-06383-y.
298 De Leeuw, A., Bukowski, K., Krijgsman, W., and Kuiper, K.F., 2010, Age of the Badenian
299 salinity crisis; Impact of Miocene climate variability on the circum-mediterranean
300 region: Geology, v. 38, p. 715–718, doi:10.1130/G30982.1.
301 Lenton, T.M., Daines, S.J., and Mills, B.J.W., 2018, COPSE reloaded: An improved model of
302 biogeochemical cycling over Phanerozoic time: Earth-Science Reviews, v. 178, p. 1–28,
303 doi:10.1016/j.earscirev.2017.12.004.
304 Mandic, O., Sant, K., Kallanxhi, M., Ćorić, S., Theobalt, D., Grunert, P., Leeuw, A. De, and
305 Krijgsman, W., 2019, Integrated bio-magnetostratigraphy of the Badenian reference
306 section Ugljevik in southern Pannonian Basin - implications for the Paratethys history (
307 middle Miocene , Central Europe): Global and Planetary Change, v. 172, p. 374–395,
308 doi:10.1016/j.gloplacha.2018.10.010.
309 Meilijson, A., Hilgen, F., Sepulveda, J., Steinberg, J., Fairbank, V., Flecker, R., Waldmann,
310 N.D., Spaulding, S.A., Bialik, O., Boudinot, F.G., Illner, P., and Makovsky, Y., 2019,
311 Chronology with a pinch of salt: Integrated stratigraphy of Messinian evaporites in the
312 deep Eastern Mediterranean reveals long-lasting halite deposition during Atlantic
313 connectivity: Earth Science Reviews, v. 194, 374-398,
314 doi:10.1016/j.earscirev.2019.05.011.
315 Mills, B.J.W., Krause, A.J., Scotese, C.R., Hill, D.J., Shields, G.A., and Lenton, T.M., 2018,
316 Modelling the long-term carbon cycle, atmospheric CO_2, and Earth surface temperature
317 from late Neoproterozoic to present day: Gondwana Research, v. 67, p. 172–186,
318 doi:10.1016/j.gr.2018.12.001.

Pérez-Asensio, J.N., Aguirre, J., Jiménez-Moreno, G., Schmiedl, G., and Civis, J., 2013, Glacioeustatic control on the origin and cessation of the Messinian salinity crisis: Global and Planetary Change, v. 111, p. 1–8, doi:10.1016/j.gloplacha.2013.08.008.

Rampino, M.R., and Caldeira, K., 2005, Major perturbation of ocean chemistry and a "Strangelove Ocean" after the end-Permian mass extinction: Terra Nova, v. 17, p. 554–559, doi:10.1111/j.1365-3121.2005.00648.x.

Rohais, S., Barrois, A., Colletta, B., and Moretti, I., 2016, Pre-salt to salt stratigraphic architecture in a rift basin : insights from a basin-scale study of the Gulf of Suez (Egypt): Arabian Journal of Geosciences, doi:10.1007/s12517-016-2327-8.

Sarmiento, J.L., and Toggweiler, J.R., 1984, A new model for the role of the oceans in determining atmospheric pCO_2: Nature, v. 308i, p. 621–624.

Shields, G.A., Mills, B.J.W., Zhu, M., Raub, T.D., Daines, S.J., and Lenton, T.M., 2019, Unique Neoproterozoic carbon isotope excursions sustained by coupled evaporite dissolution and pyrite burial: Nature Geoscience, doi:10.1038/s41561-019-0434-3.

Speranza, G., Cosentino, D., Tecce, F., and Faccenna, C., 2013, Paleoclimate reconstruction during the Messinian evaporative drawdown of the Mediterranean Basin: Insights from microthermometry on halite fluid inclusions: Geochemistry, Geophysics, Geosystems, v. 14, p. 5054–5077, doi:10.1002/2013GC004946.

Walker, J.C.G., Hays, P.B., and Kasting, J.F., 1981, A negative feedback mechanism for the long-term stabilization of Earth's surface temperature: Journal of Geophysical Research, v. 86, p. 9776, doi:10.1029/JC086iC10p09776.

Walker, J.C.G., and Kasting, J.F., 1992, Effects of fuel and forest conservation on future levels of atmospheric carbon dioxide: Global and Planetary Change, v. 5, p. 151–189, doi:10.1016/0921-8181(92)90009-Y.

Warren, J.K., 2010, Evaporites through time: Tectonic, climatic and eustatic controls in marine and nonmarine deposits: Earth-Science Reviews, doi:10.1016/j.earscirev.2009.11.004.

Wortmann, U.G., and Chernyavsky, B.M., 2007, Effect of evaporite deposition on Early Cretaceous carbon and sulphur cycling: Nature, v. 446, p. 654–656, doi:10.1038/nature05693.

Wortmann, U.G., and Paytan, A., 2012, Rapid variability of seawater chemistry over the past 130 million years: Science, v. 337, p. 334–336, doi:10.1126/science.1220656.

Yao, W., Paytan, A., Griffith, E.M., Martínez-Ruiz, F., Markovic, S., and Wortmann, U.G., 2020, A revised seawater sulfate S-isotope curve for the Eocene: Chemical Geology, v.

532, p. 119382, doi:10.1016/j.chemgeo.2019.119382.
Zachos, J.C., Dickens, G.R., and Zeebe, R.E., 2008, An early Cenozoic perspective on greenhouse warming and carbon-cycle dynamics: Nature, v. 451, p. 279–283, doi:10.1038/nature06588.
Zachos, J., Pagani, M., Sloan, L., Thomas, E., and Billups, K., 2001, Trends, Rhythms, and Aberrations in Global Climate 65 Ma to Present: Discovery Service para UNAM: Science, v. 292, p. 686–693, doi:10.1126/science.1059412.
Zeebe, R.E., and Tyrrell, T., 2019, History of carbonate ion concentration over the last 100 million years II: Revised calculations and new data: Geochimica et Cosmochimica Acta, v. 257, p. 373-392, doi:10.1016/j.gca.2019.02.041.

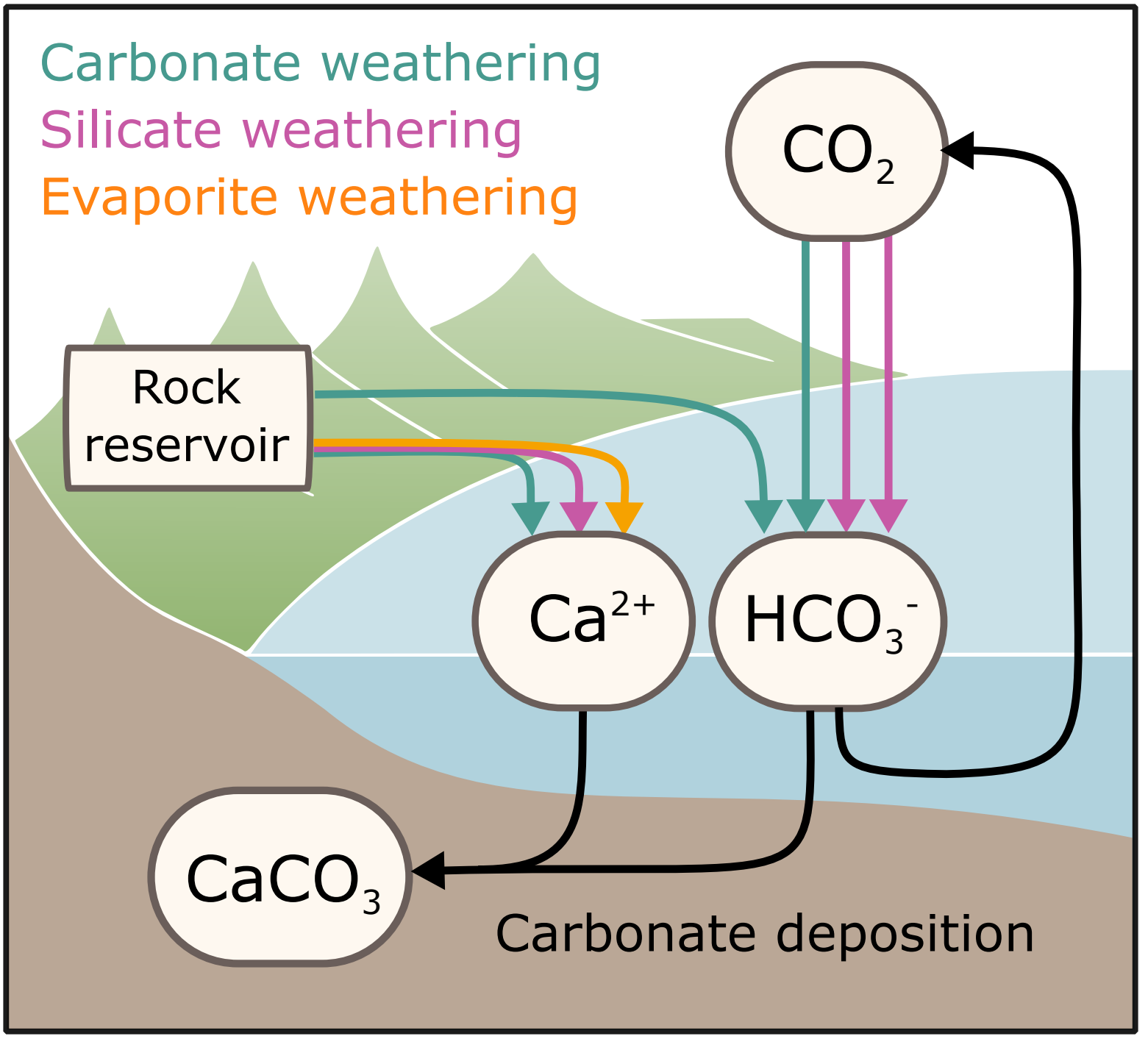
Carbonate weathering
Silicate weathering
Evaporite weathering
CO_2
Rock reservoir
Ca^{2+}
HCO_3^-
$CaCO_3$
Carbonate deposition

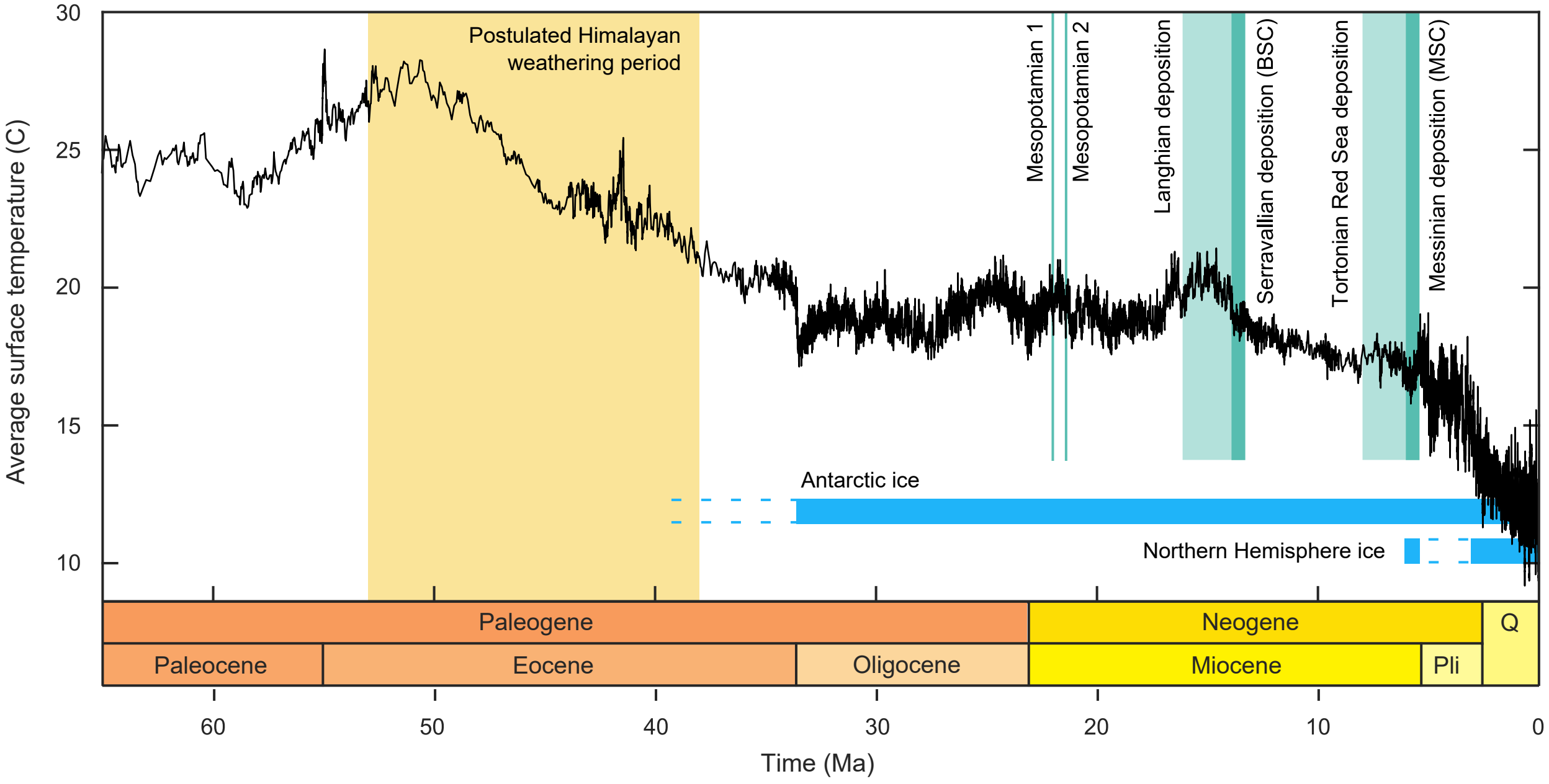
Average surface temperature (C)
30
25
20
15
10
Postulated Himalayan weathering period
Mesopotamian 1
Mesopotamian 2
Langhian deposition
Serravallian deposition (BSC)
Tortonian Red Sea deposition
Messinian deposition (MSC)
Antarctic ice
Northern Hemisphere ice
Paleogene
Neogene
Q
Paleocene
Eocene
Oligocene
Miocene
Pli
60
50
40
30
20
10
0
Time (Ma)

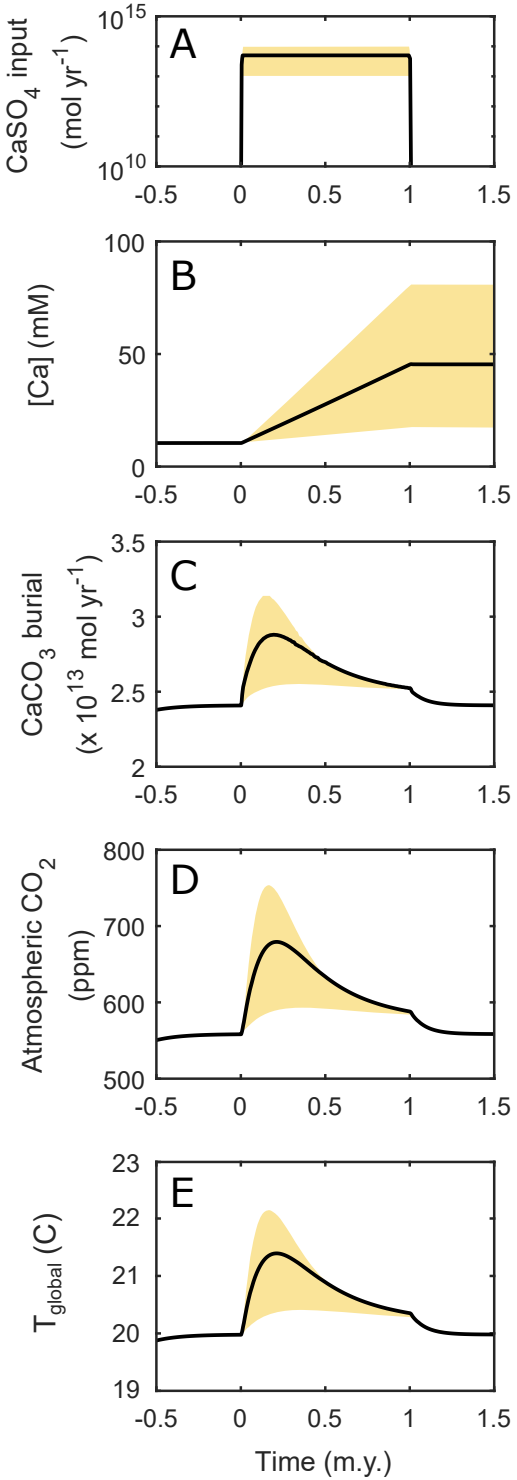
A
B
C
D
E
$CaSO_4$ input (mol yr^{-1})
10^{15}
10^{10}
[Ca] (mM)
100
50
0
$CaCO_3$ burial (x 10^{13} mol yr^{-1})
3.5
3
2.5
2
Atmospheric CO_2 (ppm)
800
700
600
500
T_{global} (C)
23
22
21
20
19
-0.5
0
0.5
1
1.5
Time (m.y.)

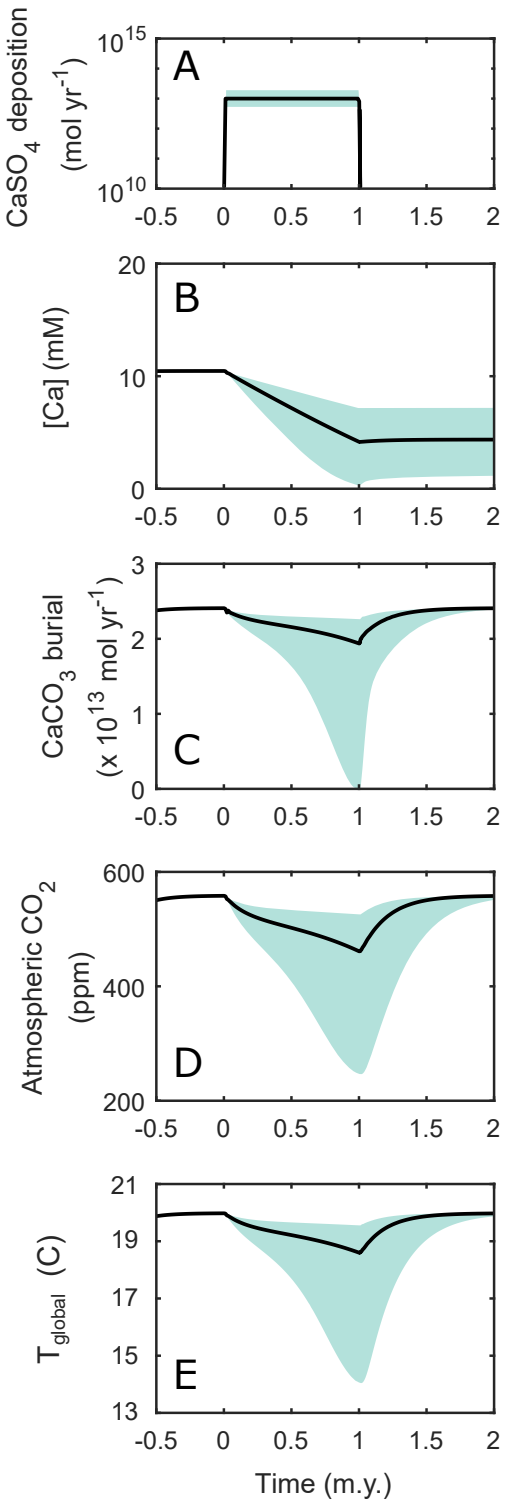
CaSO4 deposition (mol yr-1)
10^15
10^10
A
-0.5 0 0.5 1 1.5 2
[Ca] (mM)
20
10
0
B
-0.5 0 0.5 1 1.5 2
CaCO3 burial (x 10^13 mol yr-1)
3
2
1
0
C
-0.5 0 0.5 1 1.5 2
Atmospheric CO2 (ppm)
600
400
200
D
-0.5 0 0.5 1 1.5 2
Tglobal (C)
21
19
17
15
13
E
-0.5 0 0.5 1 1.5 2
Time (m.y.)